# DNS SIMULATIONS OF DROPLET MULTIPHASE FLOW IN A TWO-DIMENSIONAL CHANNEL

by
Lei Zeng

A thesis submitted to Johns Hopkins University in conformity with the requirements for the degree of Master of Science in Engineering

Baltimore, Maryland
May, 2021

# Abstract

Direct numerical simulations (DNS) are used to examine the flow of heavy drops suspended in vertical channels. The non-dimensional numbers are selected so that the drops stay nearly spherical. The imposed pressure gradient balances with the shear force and the weight of the mixture, and the system reaches hydrostatic equilibrium. Based on this force balance, the void fraction across the channel can be predicted. We used the wall shear stress and the non-dimensional root-mean-square drop distance from the centerline to determine when the system reaches a steady state. The average void fraction from the computational results matches our predicted model. For downflow, the drops are pushed to the wall and form a drop-rich region of one drop diameter thickness. For upflow, the heavy drops cluster at the center of the channel, and form a drop-free region near the wall.

## Thesis Readers

Dr. Grétar Tryggvason (Primary Advisor)
Department Head and Charles A. Miller, Jr. Distinguished Professor
Department of Mechanical Engineering
Johns Hopkins University

Dr. Jiacai Lu
Associate Research Professor
Department of Mechanical Engineering
Johns Hopkins University

# Contents

# List of Figures

# Chapter 1

# Introduction

Droplet multiphase flows are encountered in several important industrial processes. One of the common applications is the oil-water separation system. Gravity-based oil separator has been investigated both theoretically and experimentally in [1]. Because the density difference between oil drops and water is generally small, the efficiency is low relying on gravity separation followed by skimming. The oil drops are suspended in the water, so here we examine the distribution of the nearly spherical heavy drops in vertical channels with two different flow directions, determined by the imposed pressure gradient. We compare our results with the analytical model, originally developed for bubbly flows in vertical channels by Lu et al.[2].

Several numerical and experimental studies of droplet channel flows have been completed. Numerical simulations were is used to investigate the effect of different sizes on the segregation behavior for binary dispersed suspensions of fluid droplets [3]. The deformation of oil droplets adhering to channel walls was studied in [4]. Coalescence and breakup of deformable droplets dispersed in a fully turbulent channel flow were studied with a phase-field model [5], and [6] examined the droplet breakup and deformation in a statistically stationary homogeneous and isotropic turbulent flows.

The effect of the flow directions on the bubble distribution in channel flows, and

a few have also been investigated. The lift force rearranges the bubble distribution in order to balance the imposed pressure gradient [7]. Laminar bubbly flows at a steady state is well predicted by a relatively simple model in a vertical channel [2]. The behavior of bubbles in the turbulent upflow has also been studied using DNS [8], and the results from DNS and a two-fluid model are compared for bubbly flows in a two-dimensional channel [9]. Statistical learning is used to generate closure relationships for a simplified two-fluid model for bubbly flows [10].

Other authors have worked on droplet three-phase flows. A level set method has been used to study drops in three-fluid stratified flows [11], also a Smooth Particle Hydrodynamics method has been used to analyze the dynamics of a droplet on the interface between two different immiscible fluids [12].

# Chapter 2

# Numerical Method and Problem Specification

The channel is vertical with a width of $W$. The gravity acceleration $\boldsymbol{g}$ is downward so the heavy drops fall relative to the surrounding liquid. The computational domain is rectangular, with periodic boundaries in the streamwise (vertical) direction and non-slip wall boundaries in the horizontal direction.

To solve the fluid field at a given time and location, we consider an incompressible flow with two phases, governed by the Navier Stokes and continuity equations

$$\frac{\partial \rho \boldsymbol{u}}{\partial t} + \nabla \rho \boldsymbol{u}\boldsymbol{u} = -\nabla p + (\rho - \rho_{avg})\boldsymbol{g} + \nabla \cdot \mu(\nabla \boldsymbol{u} + \nabla \boldsymbol{u}^T) + \boldsymbol{f}_\sigma \quad \text{and} \quad \nabla \cdot \boldsymbol{u} = 0. \tag{2.1}$$

Here, $\boldsymbol{u}$ is the velocity, $p$ is the pressure, $\mu$ is the viscosity, $\rho$ is the density, and $\boldsymbol{f}_\sigma$ is the surface tension term.

We use the analytical model of bubbly flow in vertical channels introduced in [2]. Starting with the force balance

$$\frac{d\tau(x)}{dx} - \frac{dp}{dy} - \rho(x)g = 0, \tag{2.2}$$

where $\tau(x)$ is the shear stress. The shear force is balanced by the imposed pressure gradient and the weight of the mixture. The local density is determined by the void fraction of the drops $\rho(\varepsilon)$, $\rho = \varepsilon\rho_d + (1-\varepsilon)\rho_l$, and the average density of the domain is defined by $\rho_{av} = \varepsilon_{av}\rho_d + (1-\varepsilon_{av})\rho_l$. The subscripts $d$ and $l$ refer to the drop and the

liquid phases. The sum of the mixture weight and pressure gradient, $\beta = dp/dy + \rho_{av}g$, determines the flow direction. $\beta > 0$ results in a downflow and $\beta < 0$ creates upflow. With these relations, Eq. (2.2) becomes,

$$\frac{d\tau(x)}{dx} - \beta - \Delta\rho(\varepsilon_{av} - \varepsilon(x))g = 0, \tag{2.3}$$

where $\Delta\rho_d = \rho_l - \rho$ is a negative value because the drops are heavier than the liquid. We assume the shear vanishes in the center region of the channel, so the void fraction in the center $\varepsilon_c$ is given by

$$\varepsilon_c = \varepsilon_{av} + \frac{\beta}{g\Delta\rho}. \tag{2.4}$$

Based on this model, for downflow ($\beta > 0$), the void fraction in the center is smaller than the average because the drops accumulates near the wall region. For upflow ($\beta < 0$), drops are pushed toward the center and the void fraction in there is larger.

For downflow, we assume that the thickness of the drop-rich region near the wall is about one drop diameter $d_d$. From mass conservation, $\varepsilon_{av}W = \varepsilon_c(W - 2d_d) + 2\varepsilon_w d_d$, and by using Eq. (2.4), we have

$$\varepsilon_w = \varepsilon_{av} - \frac{\beta}{g\Delta\rho}(\frac{W}{2d_d} - 1). \tag{2.5}$$

For upflow, drops accumulate in the center region and a drop-free region is formed near the wall. The thickness of the drop-free region is $\varepsilon_{av}W = \varepsilon_c(W - 2\delta)$, and substituting into Eq. (2.4) yields

$$\delta = \frac{\beta W}{2(\beta + \varepsilon_{av}g\Delta\rho)}. \tag{2.6}$$

At steady state, the wall shear balance the net pressure gradient for both downflow and upflow, so

$$\tau_w = -\frac{\beta W}{2}. \tag{2.7}$$

To examine if the flow reaches a steady state, we use this wall shear equation, together with the root mean square of drops distance $\overline{d}$ to the channel centerline, non-dimensionalized by $\overline{d}/(\frac{W}{2})$.

The non-dimensional numbers used in multiphase systems with drops are the Morton and the Eötvös numbers,

$$M = \frac{\Delta\rho g \mu^4}{\rho_l^2 \sigma^3} \qquad Eo = \frac{\Delta\rho g d^2}{\sigma}. \tag{2.8}$$

# Chapter 3

# Results

We examine the motion of drops in a channel of size $5 \times 10$. To minimize the computational cost, we used a $256 \times 512$ grid since the grid refinement studies have shown that the results on this grid accurately describe the system. The drops have a diameter of $d_d = 0.4$, and the surface tension is $\sigma_d = 0.0002$. The density of the heavy drops is twice that of the liquid, and the drop viscosity is one-twentieth of the liquid. 50 drops are included within the domain with $Eo = 0.3$ and $M = 2.9 \times 10^{-6}$. The sign of $\beta$ determines the flow direction. The magnitude of $\beta$ should be adequately small so the drops will not coalescence. We set $\beta = 10^{-5}$ for downflow and $\beta = -10^{-5}$ for upflow. With these parameters, we initiated the flow with a parabolic velocity profile across the channel.

The drop distribution and streamline for downflow (left) and upflow (right) are presented when the flow has reached a statistically steady state at time $t = 9 \times 10^4$ (Figure 3-1). We examined the plots at different times, and found that the flow and the drop distributions are similar. With different flow directions, it is obvious that the shape and distribution of the drops are different. For downflow, the drops are pushed toward the wall and slightly deform. For upflow, drops clusters in the center region and drop-free regions are formed near the walls, and the drops stay nearly spherical. For both cases, the velocity rapidly changes near the walls.

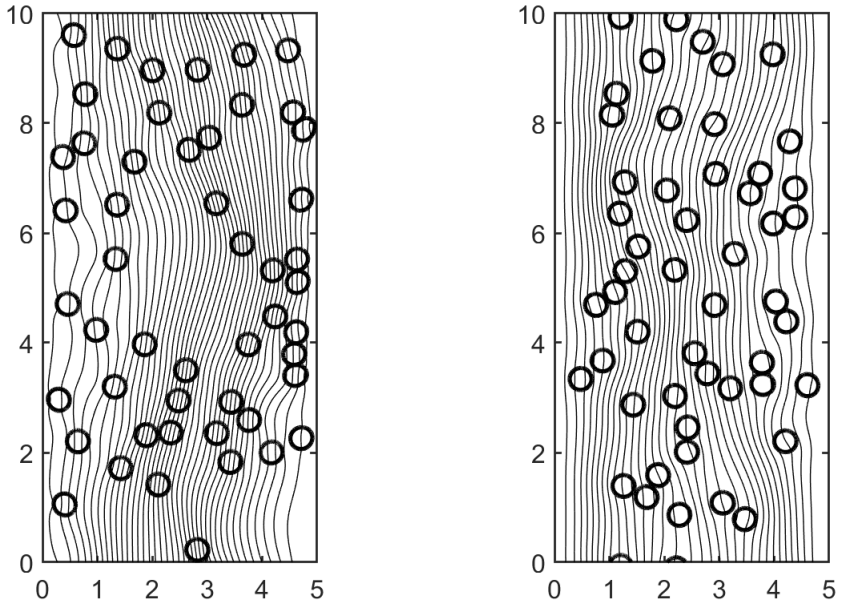


**Figure 3-1.** The drop distribution and streamlines for the downflow (left) and for the upflow (right).

We used two different methods to determine when the flow reaches the statistically steady state. First, according to Eq. (2.7), the wall shear balance out with the sum of the pressure gradient and the mixture weight across the channel. We average the wall shear $\overline{\tau_W}$ along the two non-slip walls. For both upflow and downflow, we see a big jump of the averaged wall shear stress at the early stage because of the applied parabolic velocity profile (Figure 3-2). The system reaches the statistically steady state when the averaged wall shear stress fluctuates around the predicted value $\tau_w = -\frac{\beta W}{2}$. Because downflow and upflow have opposite signs of $\beta$, we expect the predicted wall shear stress for each flow to have the same magnitude but different signs.

Furthermore, to check whether the system is at the statistically steady state, we used the non-dimensional root-mean-square (RMS) distance of drops distance from the channel centerline (Figure 3-3). Downflow has a larger value of non-dimensional RMS distance than the upflow, agreeing with our assumption that the drops gather near the wall and are far away from the channel centerline. After a transient state,

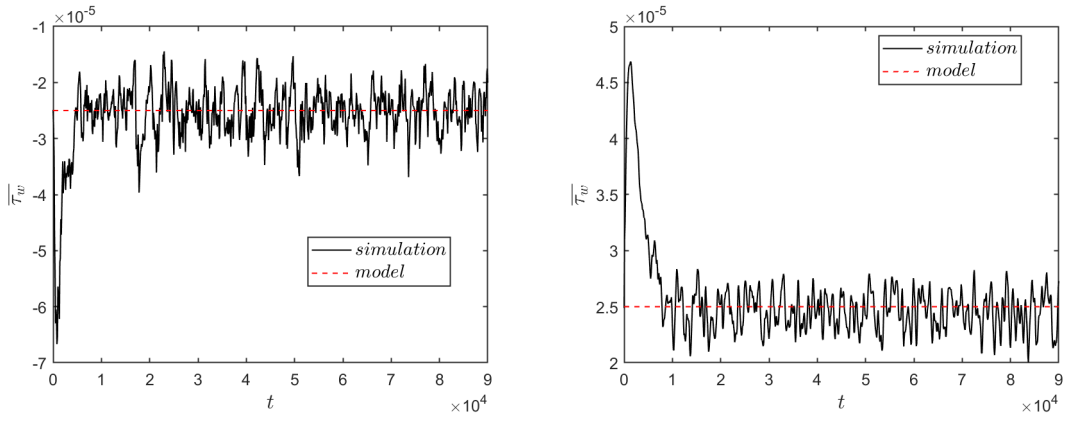


**Figure 3-2.** The averaged wall shear stress versus time for the downflow (left) and for the upflow (right).

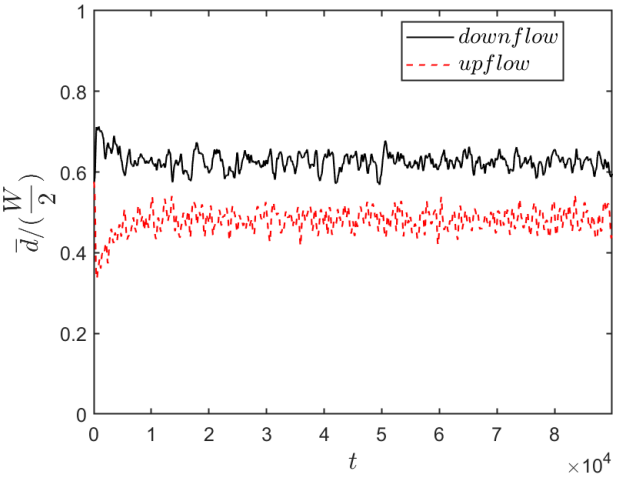


**Figure 3-3.** The non-dimensional root-mean-square distance of drops from the channel centerline.

the non-dimensional RMS distance remains relatively constant at the stationary state. The matching results of averaged wall shear stress and non-dimensional RMS distance indicate the channel flow has reached the statistically steady state at a later time. We chose $t = 3 \times 10^4$ and average until $t = 9 \times 10^4$ to compute the average steady state quantities.

We calculate the average kinetic energy versus time for both cases (Figure 3-4). The kinetic energy has a sharp increase at the initial transient state, and then remains at nearly a small constant value. Comparing the averaged value of the kinetic energy

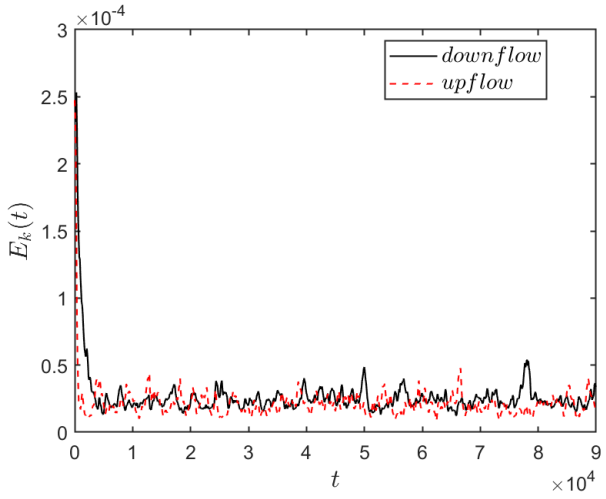


**Figure 3-4.** The average kinetic energy versus time for upflow and downflow.

from $t = 3 \times 10^4$ to $t = 9 \times 10^4$, downflow has a value 18.8% higher than the upflow. For flows with different directions, we applied the same magnitude with opposite signs of $\beta = dp/dy + \rho_{av}g$, but the upflow has to consume more energy to overcome the gravity, resulting in less average kinetic energy at the stationary state.

The average void fraction over the vertical direction of the channel by averaging over the statistically steady state time from $t = 3 \times 10^4$ to $t = 9 \times 10^4$. We also average the right-hand side and left-hand side of the average void fraction to make the profile symmetric for flows in both directions. The void fraction versus non-dimensional cross-stream coordinate is shown in Figure 3-5. The analytical models are presented as red dashed lines. Overall, the predictions of the model fit the simulated void fraction reasonably well for both flow directions. Ideally, the drops are clustered near the wall region which is about one drop diameter thick for downflow. The simulated wall-region is slightly offset from the predicted model because drops wobble in this region and there is a minor gap of liquid between drops and walls. This gap pushes the drops toward the center region slightly, and forms a transient region between the wall and center region. For upflow, the theoretical model predicts that drops accumulate in the channel center, and form a drop-free layer near the wall. The void fraction in the

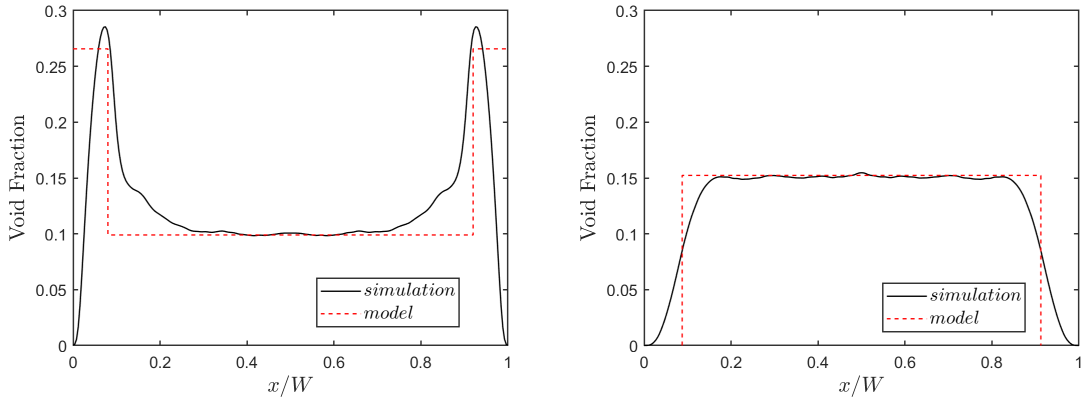


**Figure 3-5.** The averaged void fraction profile across the channel for downflow (left) and dowflow (right).

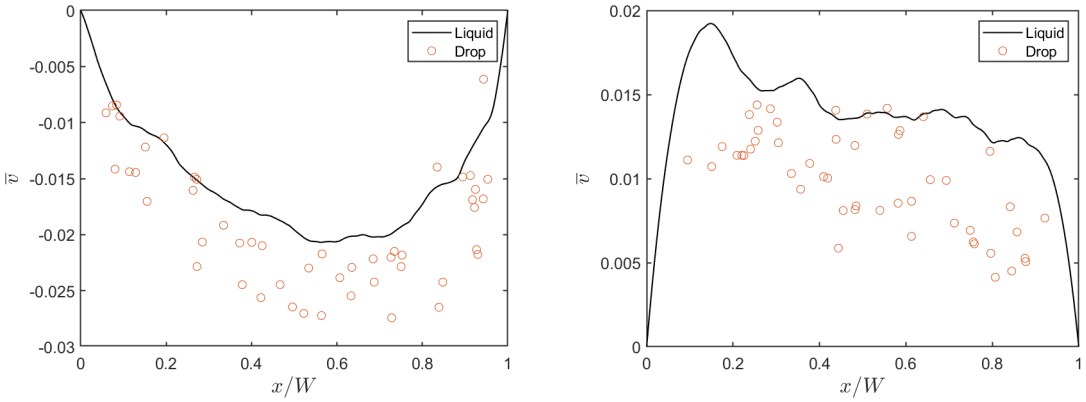


**Figure 3-6.** The averaged drop and liquid vertical velocity across the channel at $t = 9\times10^4$ for downflow (left) and upflow (right).

center $\varepsilon_c$ is well predicted with small fluctuation. From the simulation, the wall-region is not perfectly drop-free, which causes a small transient region as well.

The averaged drop and liquid vertical velocity across the channel, versus the non-dimensional cross-stream coordinate at $t = 9 \times 10^4$ for both flow directions is shown in Figure 3-6. The solid line is the liquid velocity, and each circle denotes a drop velocity at that non-dimensional location. It is obvious that most of the 50 drops have a higher velocity than the surrounding fluid for the downflow, and lower velocity for the upflow. The downflow velocity profile is slightly more symmetric than the upflow profile.

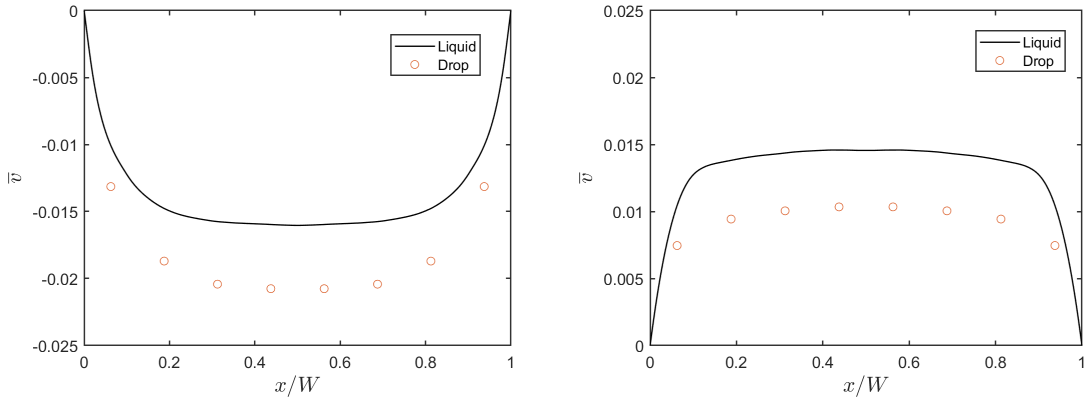


**Figure 3-7.** The time averaged drop and liquid vertical velocity across the channel for downflow (left) and upflow (right). The results are averaged from $t = 3 \times 10^4$ to $t = 9 \times 10^4$

The vertical liquid velocity averaged over a period of time in the same way as the void fraction is shown in Figure 3-5. We divide the channel into eight equal width bins, and average the drop velocity for each bin which is presented by the red circles (Figure 3-7). The drops and the liquid velocity are lower near the wall than in the center because the wall shear slows down the flow. The drops fall relative to the surrounding liquid, so drops have higher vertical velocity than liquid for downflow and lower velocity for upflow. Both the drop and the liquid velocities are higher in downflow than in upflow, and this result matches with the higher value of kinetic energy in the downflow.

# Chapter 4

# Conclusion

We use direct numerical simulation to examine droplet multiphase flow in a vertical channel for two different flow directions caused by the imposed pressure gradient. To determine whether the systems have reached a statistically steady state we have used the averaged wall shear stress and the non-dimensional root-mean-square distance of drops from the channel centerline. Both quantities indicate that the flow reaches a stationary state after a sharp change during the initial transient state.

We also found that the time averaged kinetic energy is higher for the downflow than the upflow after the flow approaches the steady state. These results correspond with our time averaged vertical velocities of drops and liquid across the channel. We then compare our results with the predictions of a simple theoretical model, originally developed for bubbly multiphase flows. The theoretical void fraction models fits our simulation results for both flow directions but with a small transient region between the wall and the center regions. In the center region of the channel, the void fraction is nearly uniform. In the wall regions, the drops are pushed toward the walls for downflow and away from the wall for upflow.

The results provided a fundamental analysis of the distribution of drops suspended in channel flows, and show that the distribution of drops is reasonably well predicted by the theoretical model. Continued work will focus on combination of drop and bubble

void fraction models, which will be helpful to analyze three-phase gas-liquid-liquid system.

# References


1. Zeevalkink, J. & Brunsmann, J. Oil removal from water in parallel plate gravity-type separators. *Water Research* **17,** 365–373 (1983).
2. Lu, J., Biswas, S. & Tryggvason, G. A DNS study of laminar bubbly flows in a vertical channel. *International Journal of Multiphase Flow* **32,** 643–660 (2006).
3. Makino, M. & Sugihara-Seki, M. Segregation by size difference in binary suspensions of fluid droplets in channel flow. *Biorheology* **50,** 149–163 (2013).
4. Seevaratnam, G., Ding, H., Michel, O., Heng, J. & Matar, O. Laminar flow deformation of a droplet adhering to a wall in a channel. *Chemical Engineering Science* **65,** 4523–4534 (2010).
5. Scarbolo, L., Bianco, F. & Soldati, A. Coalescence and breakup of large droplets in turbulent channel flow. *Physics of Fluids* **27,** 073302 (2015).
6. Perlekar, P., Biferale, L., Sbragaglia, M., Srivastava, S. & Toschi, F. Droplet size distribution in homogeneous isotropic turbulence. *Physics of Fluids* **24,** 065101 (2012).
7. Azpitarte, O. & Buscaglia, G. Analytical and numerical evaluation of two-fluid model solutions for laminar fully developed bubbly two-phase flows. *Chemical Engineering Science* **58,** 3765–3776 (2003).
8. Lu, J. & Tryggvason, G. Dynamics of nearly spherical bubbles in a turbulent channel upflow. *Journal of Fluid Mechanics* **732,** 166–189 (2013).
9. Biswas, S., Esmaeeli, A. & Tryggvason, G. Comparison of results from DNS of bubbly flows with a two-fluid model for two-dimensional laminar flows. *International Journal of Multiphase Flow* **31,** 1036–1048 (2005).
10. Ma, M., Lu, J. & Tryggvason, G. Using statistical learning to close two-fluid multiphase flow equations for bubbly flows in vertical channels. *International Journal of Multiphase Flow* **85,** 336–347 (2016).
11. Li, H., Yap, Y., Lou, J. & Shang, Z. Numerical modelling of three-fluid flow using the level-set method. *Chemical Engineering Science* **126,** 224–236 (2015).
12. Tofighi, N. & Yildiz, M. Numerical simulation of single droplet dynamics in three-phase flows using ISPH. *Computers  Mathematics with Applications* **66,** 525–536 (2013).

# Appendix I

# Numerical Studies of Disperse Three Phase Fluid Flows

# Numerical Studies of Disperse Three Phase Fluid Flows

Lei Zeng, Daniel Velez, Jiacai Lu, and Grétar Tryggvason

Department of Mechanical Engineering, Johns Hopkins University, MD, USA

May 9, 2021

**Abstract**

The dynamics of a three-phase gas-liquid-liquid multiphase system is examine by direct numerical simulations. The system consists of a continuous liquid phase, buoyant gas bubbles and smaller heavy drops that fall relative to the continuous liquid. The computational domain is fully periodic and a force equal to the weight of the mixture is added to keep it in place. The governing parameters are selected so that the terminal Reynolds numbers of the bubbles and the drops are moderate and while the effect of bubble deformability is examined by changing its surface tension, the surface tension for the drops is sufficiently high so they do not deform. The dependency of the slip velocities, the velocity fluctuations, as well as the distribution of the dispersed phases, on the volume fraction of each phase are examined. It is found that while the distribution of drops around a single three-dimensional bubble is uneven and depends on its deformability, the distribution of drops around freely interacting bubbles in two-dimensions is relatively uniform, for the parameters examine here.

## 1 Introduction

The dynamics of a three phase gas-liquid-liquid multiphase system, is examined by direct numerical simulations, where the continuum equations describing fluid flows are solved sufficiently accurately so that every length and time scale are fully resolved, for unsteady systems. The system consists of a continuous liquid phase, buoyant gas bubbles that rise and heavy drops that fall, relative to the continuous liquid. Three-phase gas-liquid-liquid systems are found in many engineering applications. One of the more common one consists of gas bubbles and oil drops in water as found in, for example, water management in the oil industry and the separation of oil and grease from municipal and industrial waste water. The density difference between oil and water is generally small, so separation relying on gravity driven settling is slow. However, by injecting gas bubbles into the mixture that stick to the oil drops and carry them to the top, the rate of separation can be greatly increased. While the collision of bubbles and drops and their subsequent interactions, such

as when an oil drop engulfs an air bubble, is critical to the efficiency of the process, here we focus on the pre-collision stage where the drops do not stick to the bubbles. For a relatively recent review of gas flotation see Saththasivam et al. [2016] and discussions of the capture of an oil drop by a gas bubble can be found in Torza and Mason [1970], Moosai and Dawe [2003], Yan et al. [2020], for example. Oil-water-gas flows are also found in many other circumstances, such as in oil wells and pipeline (Yaqub et al. [2020]).

Numerical simulations, particularly direct numerical simulations, have come a long way in the last two decades. Early simulations of many interacting bubbles can be found in Bunner and Tryggvason [2002] who examined bubbles in initially quiescent liquid in fully periodic domains, and more recent studies include Lu and Tryggvason [2013], du Cluzeau et al. [2019] where the dynamics of bubbles in turbulent channel flows is examined. While a large number of authors have examined the dynamics of two-phase flows, fully resolved numerical simulations of three-phase systems are relatively rare and usually concerned with systems different from the one considered here. Those include simulations of bubbles and drops in minichannels using a volume of fluid method by Rajesh and Buwa [2018]; Li et al. [2015] who use a level set method to study drops in two-layer stratified flows; and Tofighi and Yildiz [2013] who examined the dynamics of a drop on the interface between two different fluids, using Smooth Particle Hydrodynamics. The only studies that we have found of the dynamics of fully resolved bubbles and drops are Dinariev and Evseev [2018] who use a method that they refer to as density functional hydrodynamics. They present several pictures of the interaction of a few bubbles with a few drops, but no quantitative information.

While the focus here is on the interactions of buoyant bubbles with heavy drops, we expect the dynamics before collision to be similar to the interaction of spherical solid particles with bubbles, such as in froth flotation for mineral processing and recycling of plastics, where hydrophobic particles stick to bubbles and are carried to the top of the mixture and removed (King [2012], Pita and Castilho. [2017]). Most simulations of such systems involve considerable simplifications such as where the bubbles are fully resolved and the flow around them but the solid phase modeled as point particles. van Sint Annaland et al. [2005] simulated the motion of bubbles in initially quiescent flow using a front tracking method to track the bubble surface but modeling the particles as point particles, with two-way coupling. The bubbles were initially put in the lower part of the computational domain, which contained a large number of particles and the simulations examined how particles were transported in the wake of the bubbles, as they left the particle rich region. A similar study was done by Liu and Luo [2018], who simulated the motion of one and two bubbles and their interactions with point particles, using a VOF method to represent the bubble. Those studies where, however, limited to two-dimensional flows. Other authors have focused on the interaction of a single bubble with point particles. Those include Lecrivain et al. [2016] who captured the bubble by a phase field method and Bogner et al. [2018] who used an LBM method. Liu and Schwarz [2009a,b] studied the influence of turbulence on the interaction of several point particles with a single bubble, but used a $k-\epsilon$ models

for the turbulence, rather than fully resolving the flow. In some cases, the bubbles are also modeled as point particles, such as by Fayed and Ragab [2013] who simulated turbulent flow with bubbles and solid particles that were both modeled as point particles using one-way coupling where the disperse phases did not affect the carrier phase. Similarly, a discrete element method has been used to examine the interaction of several point particles with one bubble in Maxwell et al. [2012], Gao et al. [2014]. The only simulations that we are aware of, where both the bubbles and the solid particles are resolved, are Baltussen et al. [2013] and Sasic et al. [2014] who capture the bubbles by a volume-of-fluid (VOF) method and use an immersed boundary method (IBM) for the solid particles. Modeling of three phase systems using Euler-Euler models for the average flow are more common. For bubbles and drops see, for example, Cazarez et al. [2010] and for bubbles and solid particles see the extensive review by Wang et al. [2018].

## 2 Numerical Method and Problem Specification

We consider incompressible flow consisting of different fluids or phases, evolving in time, governed by the Navier Stokes equations

$$\frac{\partial \rho \boldsymbol{u}}{\partial t} + \nabla \rho \boldsymbol{u}\boldsymbol{u} = -\nabla p + (\rho - \rho_{avg})\boldsymbol{g} + \nabla \cdot \mu(\nabla \boldsymbol{u} + \nabla \boldsymbol{u}^T) + \boldsymbol{f}_\sigma \quad \text{and} \quad \nabla \cdot \boldsymbol{u} = 0. \tag{1}$$

Here, $\boldsymbol{u}$ is the velocity, $p$ is the pressure, $\rho$ is the density, $\mu$ is the viscosity, $\boldsymbol{g}$ is the gravity acceleration and $\boldsymbol{f}_\sigma$ is the surface tension term. Solving these equations accurately gives the fully resolved flow field at any given time and spatial location. To identify the different phases we define two index or marker functions, $\chi_g$ to identify the gas phase and $\chi_d$ to identify the heavy droplet phase.

$$\chi_g(\boldsymbol{x}) = \begin{cases} 0 \text{ in the liquid} \\ 1 \text{ in the bubbles} \end{cases}, \qquad \chi_d(\boldsymbol{x}) = \begin{cases} 0 \text{ in the liquid} \\ 1 \text{ in the drops.} \end{cases} \tag{2}$$

The various flow quantities, such as density and viscosity can then be written as

$$\phi_i = \phi_l + (\phi_i - \phi_l)\chi_i \tag{3}$$

where $\phi_l$ is the property of the continuous liquid and $i = g$ for the bubbles and $i = d$ for the drops. Surface tension is assigned to each interface point and is different for the bubbles and the drops.

The governing equations are solved using an explicit second order finite volume projection method on a staggered fixed regular grid. The advection terms are approximated by a QUICK upwind scheme and the viscous terms by a centered scheme. To update the marker function, and thus the material properties, we represent the interfaces between different fluids by connected marker points (usually called front) that move with the fluid velocity. The marker function is then constructed from the location of the marker points. Surface

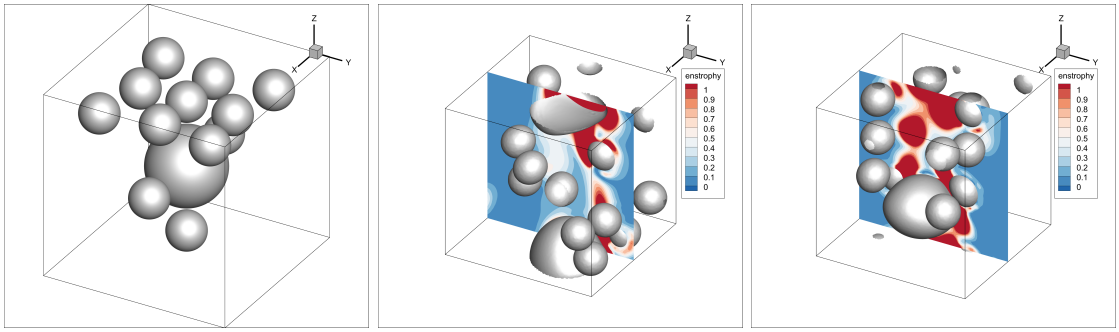


Figure 1: A bubble and 12 drops at time 0 (left frame) and 100 for $Eo = 2$ (middle frame)and $Eo = 10$ (right frame). The enstropy is shown in a plane cutting through the center of the domain, for the later times.

tension is computed on the front and transferred to the fixed grid and added to the discrete Navier-Stokes equations. For a detailed description of the method and various verification tests, see Tryggvason et al. [2011].

The computational domain is a hexahedron in 3D and rectangle in 2D, with periodic boundaries in all directions and to prevent the system from "falling" due to gravity, we add a positive upwards force equal to the weight of the mixture ($\rho_{avg}\boldsymbol{g}$).

The dynamics of systems with bubbles or drops is usually described by the Morton and the Eötvös numbers, defined by

$$M = \frac{\Delta\rho g\mu^4}{\rho^2\sigma^3} \qquad Eo = \frac{\Delta\rho g d^2}{\sigma}. \tag{4}$$

For our system we need to specify those for both the bubbles and the drops. In addition, the volume fraction is generally needed for multiphase systems and here, where we work with bubbles and drops of specific sizes, we report the number of bubbles $N_b$ and number of drops $N_d$.

# 3 Results

## 3.1 One 3D bubble and several drops

We start by examining the motion of one relatively large bubble and several smaller drops in a cubical computational domain with side lengths equal to 1, resolved by a $64^3$ grid. The bubbles have a diameter $d_b = 0.4$ and the droplets have diameters $d_d = 0.2$. The density and viscosity of the continuous fluid are $\rho_l = 1.0$ and $\mu = 0.009$, respectively, for the bubble we have $\rho_d = 0.05$ and $\mu_b = 0.0005$ and for the drops $\rho_d = 2.0$ and $\mu_b = 0.016$. Surface tension is $\sigma_d = 0.01$ for the drop-liquid interface but the surface tension for the

| $\sigma$ | 0.04 | 0.01 | 0.00067 | 0.004 | 0.002 |
|---|---|---|---|---|---|
| $Eo_b$ | 0.5 | 2.0 | 3.0 | 5.0 | 10.0 |
| $M_b$ | $3.1 \times 10^{-8}$ | $2.0 \times 10^{-6}$ | $6.7 \times 10^{-6}$ | $3.1 \times 10^{-5}$ | $2.5 \times 10^{-4}$ |

Table 1: The surface tension for the bubbles and the corresponding $Eo_b$ and $M_b$.

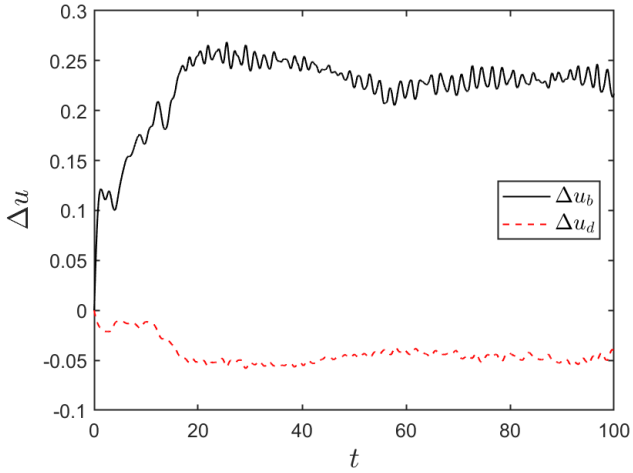


Figure 2: The slip velocity versus time for $Eo = 2$ and $N_d = 12$.

bubble-liquid interface is varied, resulting in different Morton and the Eötvös numbers as shown in Table 1. While the grid resolution is relatively low, grid refinement studies have confirmed that the results are reasonably accurate and correctly describe the dynamics of the system. The number of drops is varied and we show results for $N_d = [12, 16, 20]$. The simulations were run up to time 100, at which time the bubble had passes about twenty times through the computational domain.

Figure 1 shows the bubble and twelve drops at time zero and time 100 for $Eo = 2.0$ and $Eo = 10.0$. For the lower Eötvös number the bubble deforms only slightly as it rises but for the higher one more deformation are seen. The drops remain essentially spherical. The results for $Eo = 0.5$ are similar to the $Eo = 2.0$ case and the $Eo = 5.0$ results fall in-between the $Eo = 2.0$ and the $Eo = 10.0$ case. In addition to the bubble and the drops, the enstropy ($\boldsymbol{\omega} \cdot \boldsymbol{\omega}$) is plotted in a plane cutting through the middle of the domain. The highest values are ahead and behind the bubble spanning the region between the bubble in one period and the next one, suggesting it is the wake of the bubbles that produces the strongest vorticity.

The velocity of the bubble and the drops are plotted versus time for $Eo = 2.0$ and $N_d = 12$ in figure 1. The bubble wobbles slightly as it rises as is seen in the nearly periodic oscillations in the rise velocity. For the drops we plot the average velocity, which is negative

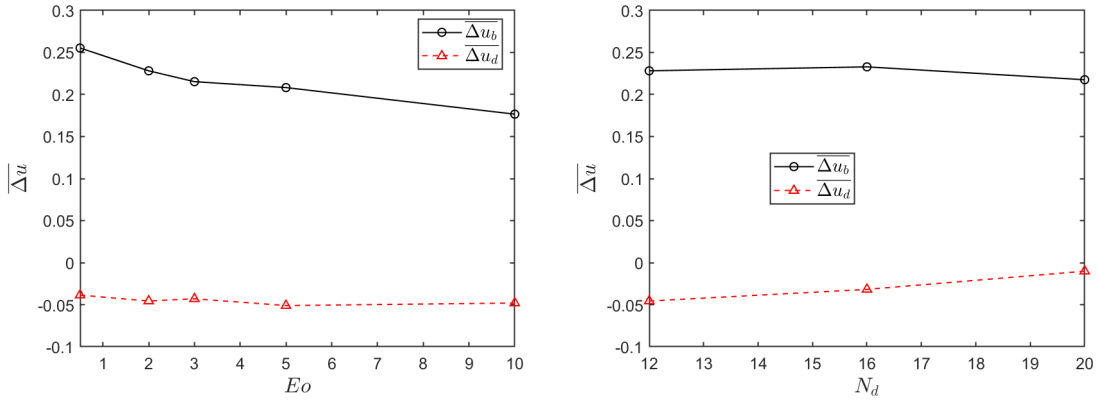


Figure 3: The slip velocity versus bubble Eötvös number for $N_d = 12$ (left) and versus number of drops for $Eo = 2$ (right).

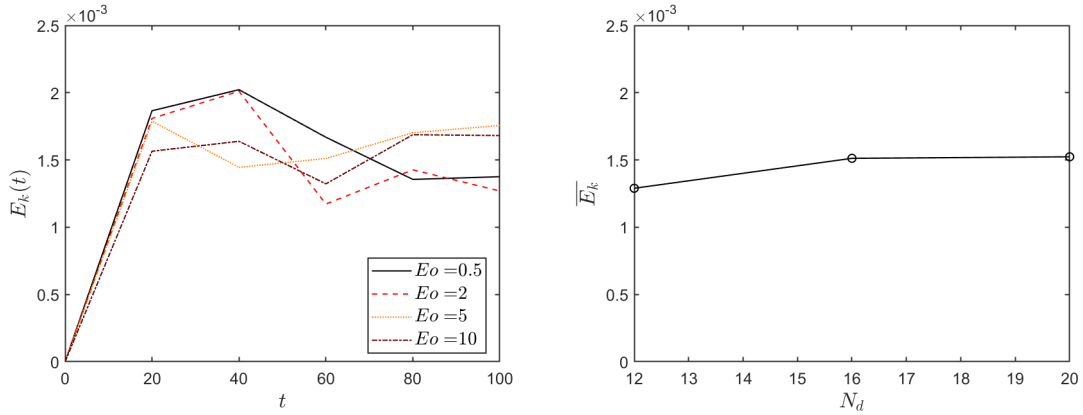


Figure 4: The average kinetic energy versus time for $N_d = 12$ and several Eötvös numbers (left). The average kinetic energy versus the number of drops $N_d$ for $Eo = 2.0$.

and relatively steady. After the initial transient the system reaches an approximately stationary state where the average motion does not change. When we compute average steady state quantities for the system (shown below) we start at time $t = 50$ and average until the last time simulated ($t = 100$). Results for other bubble Eötvös numbers and different number of drops are similar.

The slip velocity between the bubble and the continuous liquid and between the heavy drops and the continuous liquid averaged over time after the systems reaches an approximate stationary state are shown in figure 3(a) versus Eötvös number of the bubble ($Eo_b$) and $N_d = 12$. It is clear that while the droplet velocity remains nearly unchanged, the bubble slows down slightly as it becomes more deformable, although the decrease is relatively small. Figure 3(b) shows the averaged rise velocity for different numbers of drops for $Eo = 2.0$ and while the bubble velocity is only minimally affected, the velocity of the drops decreases slightly as their number is increased.

In figure 4 we examine the velocity fluctuations in the liquid by plotting the kinetic energy versus time for four Eötvös numbers on the left and the average kinetic energy versus number of drops for $Eo = 2$ in the right frame. In all cases we see that after an initial sharp rise, the kinetic energy remains relatively constant and after averaging over time the kinetic energy shows only a very weak dependency on the number of drops. Similar results are seen for other Eötvös numbers.

One of the main questions in many applications of disperse three phase flows is how the drops (or solids) and the bubbles interact. In wastewater remediation the efficiency on the process depends critically on the bubbles colliding with and capturing droplets, and the same is true for flotation in mineral processing, where the drops are replaced by solid particles. To examine how the droplets are distributed around the bubble, we show the angular and radial location of droplets with respect to the bubble in figure 6 at twenty equispaced times, for twelve drops ($N_d = 12$). Data for $Eo = 0.5$ are shown on the left and for $Eo = 10$ on the right. In both cases the drops move past the bubble, with essentially no drops directly ahead or behind the bubble, but for the nearly spherical bubble the drops are clustered in a relatively narrow column that almost touches the bubble since the sum of the bubble and drop radii is $R_b + R_d = 0.3$. For the more deformable bubble the column is more spread out and we see more drops closer to the centerline in front of the bubble. Since the high $Eo$ bubble becomes relatively "flat" as it rises, some of the drops in the front get close its center.

To examine the droplet distribution in more detail, we show the weighted average radial and angular distribution in figure 6. Since the volume of a torus around the bubble depends on the distance from the centerline, we divide the average number of drops in a volume element by the distance from the centerline. To produce a continuous curve, we apply kernel smoothing, where the width of the kernel is selected by trial and error. The left frame shows the radial distribution, averaged over the azimuthal direction. For the lowest $Eo$ there is a distinct maximum at $r = 0.3$, as also seen in figure 5 and for the highest $Eo$ the distribution reaches close to the origin, corresponding to the drops ahead and close

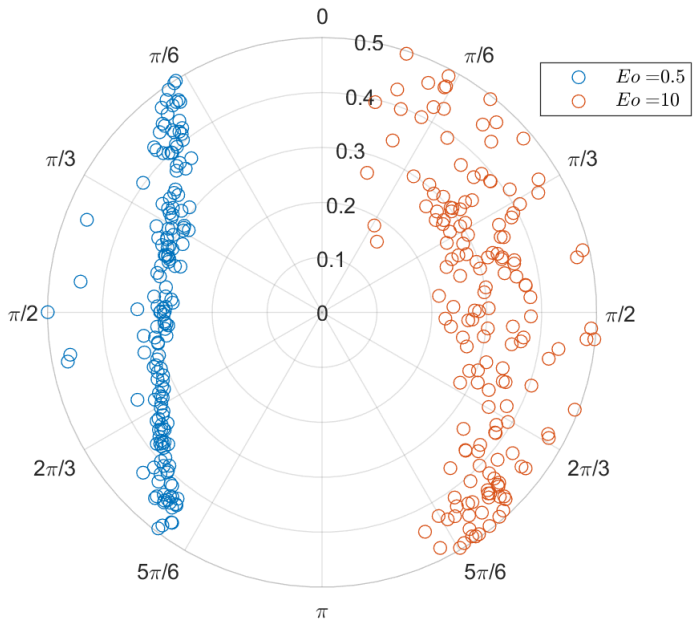


Figure 5: The relative location of the drops for 20 time samples for $N_d = 12$. $Eo = 0.5$ on the right and $Eo = 10$ on the left.

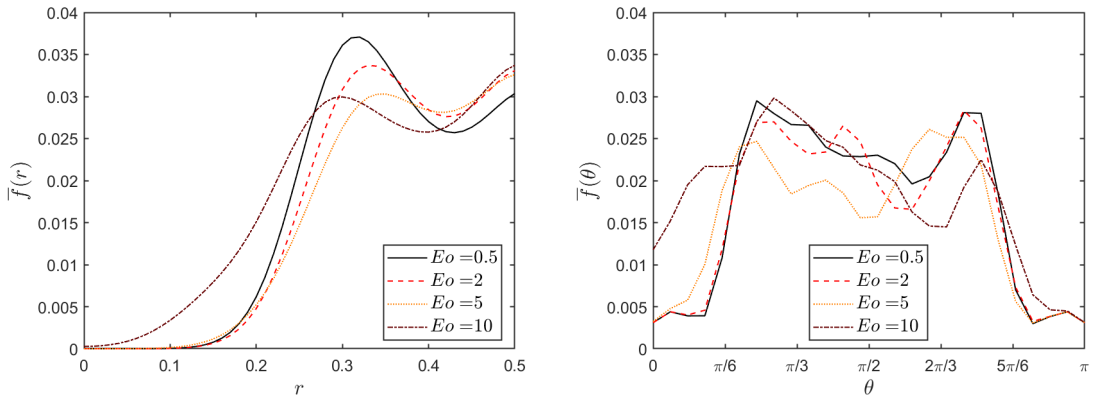


Figure 6: The angular average pair distribution function versus distance from the bubble center (left) and radially average pair distribution function versus angle, measured from the top of the bubble (right).

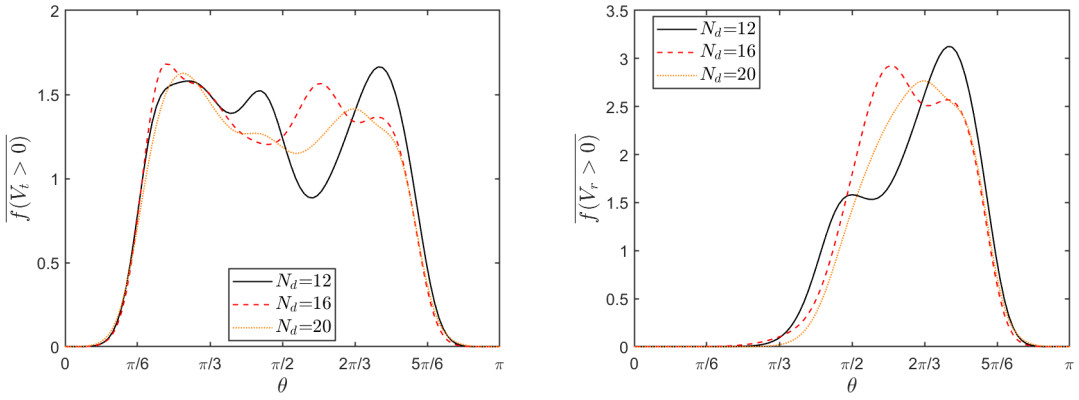


Figure 7: The probability that the relative tangential (left) and radial (right)velocities of the drops next to the bubble are positive, for $Eo = 2.0$ and different number of drops.

to the bubble. The angular distribution, averaged for $r < 0.5$ is shown in the right frame and it is clear that for the lower $Eo$s the distribution is highest at around $\theta = \pi/5$ then gradually deceasing but with a peak at around $\theta = 4\pi/5$. At the poles we see very low values, consistent with the left hand side of figure 5. For the highest $Eo$ the distribution is more uniform, but while there is a low value at the back, the value at $\theta = 0$ is significantly higher than for the other cases.

In figure 7 we examine the relative velocity between the bubble and the drops by plotting the probability that the relative tangential velocity (left frame) and the relative radial (right frame) velocity are positive, following Bunner and Tryggvason [2002]. The tangential velocity is taken to be positive if the drop is moving towards the back of the bubble and the radial velocities is positive if the drops move away from the bubble. In all cases the plot on the left shows that the drops slide along the bubble surface from the front to the back, as expected. Similarly, the plot on the right shows that the drops are likely to be moving away from the bubble near its back. The results for the fewest drops ($N_d = 12$) are slightly different than for the larger numbers, showing a dip just below the equator for the tangential velocities and a rapid rise of the probability that the drops are moving away for the radial velocities.

### 3.2 Several bubbles and drops in 2D flows

While examination of the interaction of several drops with one bubble in a "unit cell" allows us to study some aspect of the system, in real systems we expect to have several bubbles and several drops. While we have not examined the case of many bubbles and many drops in fully three-dimensional flows yet, we have done a few simulations of two-dimensional flows with four large bubbles and several smaller drops. The parameters the

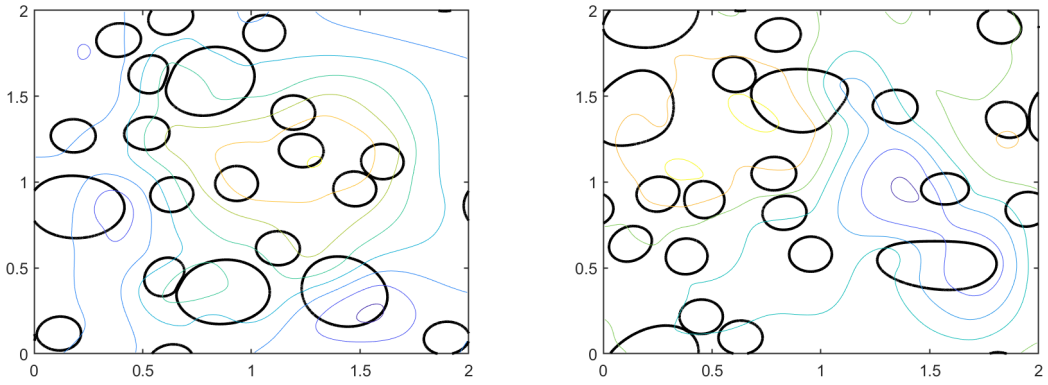


Figure 8: The bubbles and drops, along with a few streamlines, at $t = 500$ from two simulations of four large bubbles and sixteen small drops. For the bubbles $Eo_b = 1$ in the left frame and $Eo_b = 3$ in the right frame.

same as in the previous section and the bubble surface tension is varied to give different Eötvös and Morton numbers. The simulations are run up to time $t = 1000$ at which times the bubbles have moved fifty times through the domain, on the average. Figure 8 shows the solution at $t = 500$, for $Eo_b = 1.0$ (left frame) and $Eo_b = 30$ (right frame). In addition to showing the bubbles and the drops, we also show a few streamlines in a stationary frame of reference. An examination of those plots, as well as others at different times, show that overall the flows are relatively similar. Both the bubbles are the drops are distributed throughout the domain, although small clusters of drops are often seen, such as here. Similarly, although sometime the bubbles collide with each other, persistent clusters or "streams" as sometimes found for deformable bubbles in fully three-dimensional flows, due to the differences in lift on a spherical and deformable bubbles (Bunner and Tryggvason [2003], Ervin and Tryggvason [1997]), are not seen. We also note that the flow field consists of relatively large regions of recirculating flows, as generally seen for two-dimensional flows, including those with bubblys (Esmaeeli and Tryggvason [1996]).

The slip velocity between the bubbles and the continuous liquid and the drops and the continuous liquid, averaged over the different bubbles and the drops, is shown in figure 9 versus time for $Eo_b = 1$ (left frame) and the time average of the slip velocities is shown in the right frame for $Eo_b = 2$, versus the number of drops $N_d$. The bubbles rise due to buoyancy so their slip velocity is positive, while the drops are denser than the continuous liquid and fall down with a negative slip velocity. The left frame shows that the flow reaches a statistically stationary state very quickly and that the average bubble slip velocity fluctuates greatly. This is presumably due to the relatively small size of the system, both in terms of number of bubbles and domain size. However, even in a larger system where the average over all the bubbles might be smaller, we still expect individual bubbles to

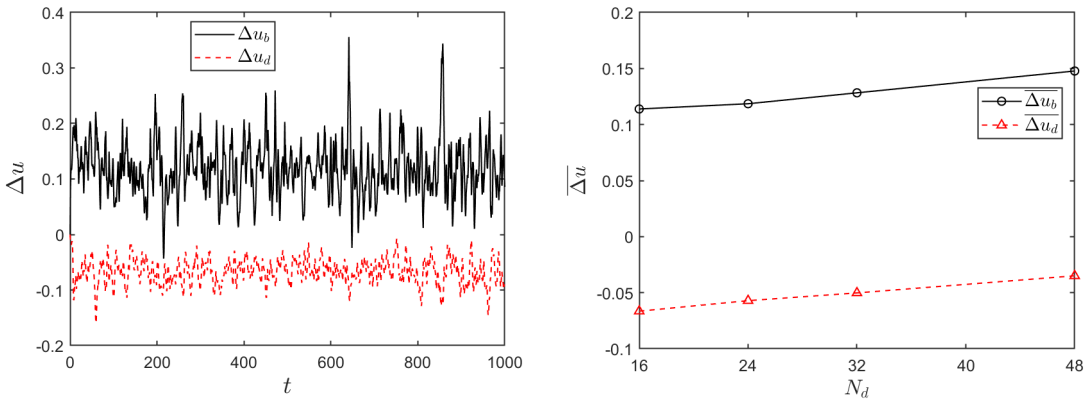


Figure 9: Slip velocity for the bubbles the drops. The slip velocity versus time for $Eo_b = 1$ (left frame) and the time averaged slip velocity for $Eo_b = 2$ versus the number of drops $N_b$ (right frame).

move very unsteadily. The slip velocity of the drops fluctuates less, in part because there are more of them so the average is better converged. As the number of drops increases, the density of the liquid mixture (continuous liquid and drops) increases so the bubble slip velocity increases slightly due to buoyancy, whereas the average drop slip velocity decreases. Plots of the slip velocity versus $Eo_b$ for a fixed $N_b$ show essentially no dependency on $Eo$. Although the flow reaches a stationary state quickly, the time average in the right frame has been computed between time $t = 500$ and $t = 1000$, using a time increment of $\Delta t = 5$. The averages discussed below have all been computed in the same way.

The time average of the kinetic energy of the continuous liquid is plotted in figure 10 versus $Eo_b$ for $N_d = 16$ (left frame) and versus $N_d$ for $Eo_b = 2$ in the right frame. The dependency on the Eötvös number is relatively weak, although it increases slightly for the most deformable bubbles. As the number of drops is increased, the kinetic energy first increases slightly but eventually it decreases as the drop volume fraction becomes sufficiently high to hinder their motion.

We have also examined the distribution of drops around each bubble in some detail. Figure 11 shows the locations of drops with respect to the centers of the bubbles at twenty evenly spaced times between $t = 500$ and $t = 1000$, for $Eo_b = 1$ on the left of the symmetry axis and for $Eo_b = 3$ on the right. It is clear that the droplets are distributed relatively uniformly around the bubbles, although there is a small region at the back with few drops, and unlike for the single three-dimensional bubble, there is little dependency on the Eötvös number, except the drops get closer to the more deformable bubble at the front. This is borne out by a more detailed analysis, such as by examining the radial distributions of the drops, shown on the right, for different $Eo_b$ and 16 drops. Here the droplet distribution in the left frame has been smoothed using a kernel function, as done in figure 5, except that for

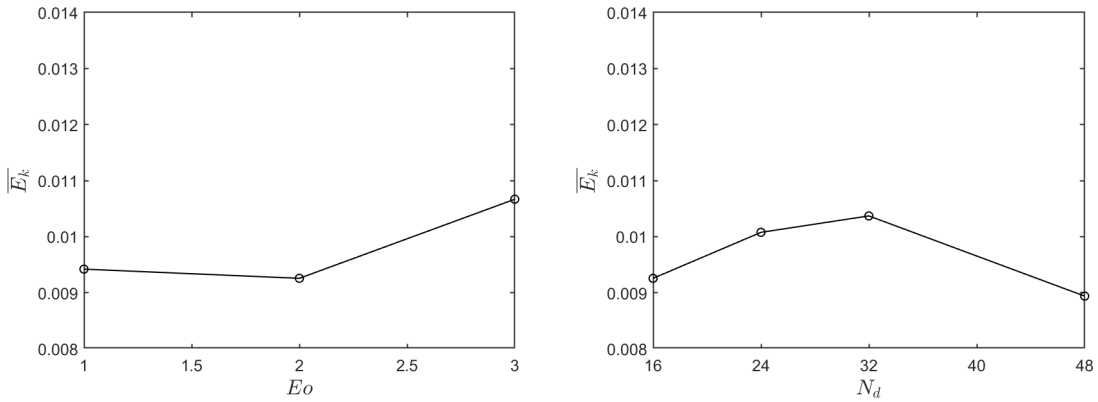


Figure 10: The kinetic energy of the liquid versus the Eötvös numbers for $N_d = 16$ (left frame) and versus the number of drops for $Eo_b = 2$ (right frame).

two-dimensional flow no volume correction to account for the azimuthal direction is needed. It is clear that first of all the distribution becomes relatively uniform immediately outside the bubble and that there are very little differences between the different Eötvös numbers. Similar plots for the angular distribution also show essentially uniform distribution that does not depend on $Eo_b$ or $N_b$.

We note that for the two-dimensional flows we have examined a much smaller range of Eötvös number then for the three-dimensional ones because at larger values the bubbles break apart, partly because of the other bubbles and also because the velocity perturbations caused by each bubble decay much slower than in three-dimensions so the interactions are more intense.

# 4 Conclusions

We have examined the dynamics of a three phase system where buoyant bubbles and heavy drops move in a continuous liquid, focusing on the dynamics of relatively small systems where the drops do not collide and stick to or engulf the bubbles. For one bubble in three-dimensional flow the results show that bubble deformability has strong impact on the dynamics and the distribution of drops around the bubble, but results for a few two-dimensional bubbles show little effect of deformability and that the drops are relatively uniformly distributed with respect to the bubbles, for the parameters examined. The number of drops does, however, have some impact on the slip velocity between the bubbles and the drops and the continuous liquid. Examining the dynamics for a system with many freely interacting three-dimensional bubbles should cast more light on the dynamics of larger systems.

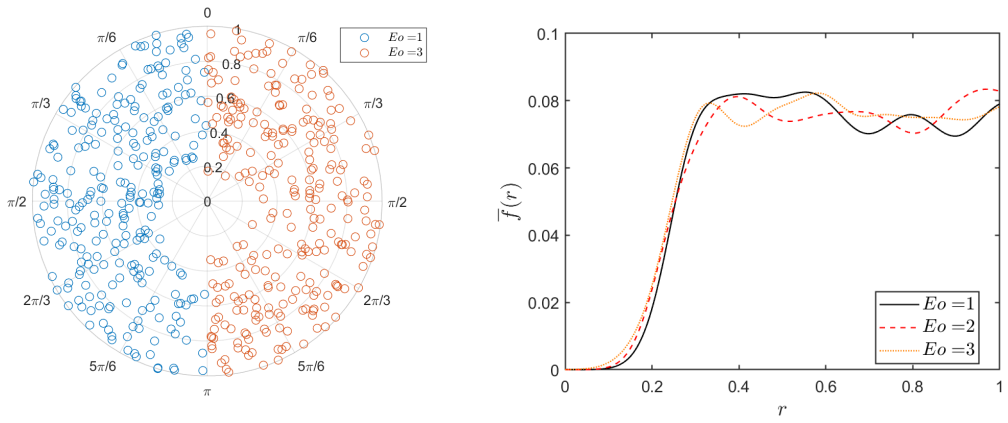


Figure 11: The location of drops with respect to bubble centers. The drops at several times are shown in the left frame for $Eo_b = 1$ (blue) and $Eo_b = 3$ (red). The radial distribution, averaged around the bubble is shown on the right, for three Eötvös numbers.

**Acknowledgement:** This research was supported in part by NSF grant CBET-2035231.

## References

M. Baltussen, L. Seelen, J. Kuipers, and N. Deen. Direct numerical simulations of gas-liquid-solid three phase flows. *Chemical Engineering Science*, 100:293–299, 2013.

S. Bogner, J. Harting, and U. Rüde. Direct simulation of liquid–gas–solid flow with a free surface lattice boltzmann method. *International Journal of Computational Fluid Dynamics*, 31:463–475, 2018.

B. Bunner and G. Tryggvason. Dynamics of homogeneous bubbly flows: Part 1. rise velocity and microstructure of the bubbles. *Journal of Fluid Mechanics*, 466:17–52, 2002.

B. Bunner and G. Tryggvason. Effect of bubble deformation on the stability and properties of bubbly flows. *Journal of Fluid Mechanics*, 495:77–118, 2003.

O. Cazarez, D. Montoya, A. Vital, and A. Bannwart. Modeling of three-phase heavy oil-water-gas bubbly flow in upward vertical pipes. *International Journal of Multiphase Flow*, 36:439–448, 2010.

O. Y. Dinariev and N. V. Evseev. Modelling of flotation processes by density functional hydrodynamics. *Minerals Engineering*, 125:239–251, 2018.

A. du Cluzeau, G. Bois, and A. Toutant. Analysis and modelling of Reynolds stresses in turbulent bubbly up-flows from direct numerical simulations. *Journal of Fluid Mechanics*, 866:132–168, 2019.

E. Ervin and G. Tryggvason. The rise of bubbles in a vertical shear flow. *ASME J. Fluid Engineering*, 119:443–449, 1997.

A. Esmaeeli and G. Tryggvason. An inverse energy cascade in two-dimensional, low Reynolds number bubbly flows. *Journal of Fluid Mechanics*, 314:315–330, 1996.

H. E. Fayed and S. A. Ragab. Direct numerical simulation of particles-bubbles collisions kernel in homogeneous isotropic turbulence. *Journal of Computational Multiphase Flows*, 5:167–188, 2013.

Y. Gao, G. M. Evans, E. J. Wanless, and R. Moreno-Atanasio. DEM simulation of single bubble flotation: Implications for the hydrophobic force in particle-bubble interactions. *Advanced Powder Technology*, 25:1177–1184, 2014.

R. King. *Modeling and Simulation of Mineral Processing Systems*. Butterworth-Heinemann, 2012.

G. Lecrivain, R. Yamamoto, U. Hampel, and T. Taniguchi. Direct numerical simulation of a particle attachment to an immersed bubble. *Physics of Fluids*, 28: https://doi.org/10.1063/1.4960627, 2016.

H. Y. Li, Y. F. Yap, J. Lou, and Z. Shang. Numerical modelling of three-fluid flow using the level-set method. *Chemical Engineering Science*, 126:224–236, 2015.

Q. Liu and Z.-H. Luo. CFD-VOF-DPM simulations of bubble rising and coalescence in low hold-up particle-liquid suspension systems. *Powder Technology*, 339:459–469, 2018.

T. Liu and M. Schwarz. CFD-based modelling of bubble-particle collision efficiency with mobile bubble surface in a turbulent environment. *Int. J. Miner. Process.*, 90:45–55, 2009a.

T. Liu and M. Schwarz. CFD-based multiscale modelling of bubble-particle collision efficiency in a turbulent flotation cell. *Chemical Engineering Science*, 64:5287–5301, 2009b.

J. Lu and G. Tryggvason. Dynamics of nearly spherical bubbles in a turbulent channel upflow. *Journal of Fluid Mechanics*, 732:166–189, 2013.

R. Maxwell, S. Ata, E. Wanless, and R. Moreno-Atanasio. Computer simulations of particle-ubble interactions and particle sliding using Discrete Element Method. *Journal of Colloid and Interface Science*, 381:1–10, 2012.

R. Moosai and R. A. Dawe. Gas attachment of oil droplets for gas flotation for oily wastewater cleanup. *Separation and Purification Technology*, 33:303–314, 2003.

F. Pita and A. Castilho. Separation of plastics by froth flotation. the role of size, shape and density of the particles. *Waste Manag.*, 60:91–99, 2017.

V. M. Rajesh and V. V. Buwa. Volume-of-fluid simulations of gas-liquid-liquid flows in minichannels. *Chemical Engineering Journal*, 345:688–705, 2018.

S. Sasic, E. K. Sibaki, and H. Ström. Direct numerical simulation of a hydrodynamic interaction between settling particles and rising microbubbles. *European Journal of Mechanics B-Fluids*, 43:65–75, 2014.

J. Saththasivam, K. Loganathan, and S. Sarp. An overview of oil-water separation using gas flotation systems. *Chemosphere*, 144:671–680, 2016.

N. Tofighi and M. Yildiz. Numerical simulation of single droplet dynamics in three-phase flows using isph. *Comput. Math. Appl.*, 66:525–536, 2013.

S. Torza and S. Mason. Three-phase interactions in shear and electrical fields. *Journal of Colloid and Interface Science*, 33:67–83, 1970.

G. Tryggvason, R. Scardovelli, and S. Zaleski. *Direct Numerical Simulations of Gas-Liquid Multiphase Flows*. Cambridge University Press, 2011. doi: https://doi.org/10.1017/CBO9780511975264.

M. van Sint Annaland, N. Deen, and J. Kuipers. Numerical simulation of gas–liquid–solid flows using a combined front tracking and discrete particle method. *Chemical Engineering Science*, 60:6188–6198, 2005.

G. Wang, L. Ge, S. Mitra, G. M. Evans, J. Joshi, and S. Chen. A review of cfd modelling studies on the flotation process. *Minerals Engineering*, 127:153–177, 2018.

S. Yan, X. Yang, Z. Bai, X. Xu, and H. Wang. Drop attachment behavior of oil droplet-gas bubble interactions during flotation. *Chemical Engineering Science*, 223:115740, 2020.

M. W. Yaqub, R. Marappagounder, R. Rusli, R. P. D.M., and R. Pendyala. Review on gas-liquid-liquid three-phase flow patterns, pressure drop, and liquid holdup in pipelines. *Chemical Engineering Research and Design*, 159:505–528, 2020.